symmetry

MDPI

Article

Social Group Optimization Supported Segmentation and Evaluation of Skin Melanoma Images

Nilanjan Dey [1], Venkatesan Rajinikanth [2], Amira S. Ashour [3] and João Manuel R. S. Tavares [4,*]

[1] Department of Information Technology, Techno India College of Technology, Kolkata 700156, West Bengal, India; neelanjan.dey@gmail.com

[2] Department of Electronics and Instrumentation Engineering, St. Joseph's College of Engineering, Chennai 600119, Tamilnadu, India; rajinikanthv@st.josephs.ac.in

[3] Department of Electronics and Electrical Communications Engineering, Faculty of Engineering, Tanta University, Tanta 31527, Egypt; amirasashour@yahoo.com

[4] Instituto de Ciência e Inovação em Engenharia Mecânica e Engenharia Industrial, Departamento de Engenharia Mecânica, Faculdade de Engenharia, Universidade do Porto, Porto, Rua Dr. Roberto Frias s/n, 4200-465 Porto, Portugal

* Correspondence: tavares@fe.up.pt; Tel.: +351-22-508-1487

Received: 8 January 2018; Accepted: 15 February 2018; Published: 22 February 2018

Abstract: The segmentation of medical images by computational methods has been claimed by the medical community, which has promoted the development of several algorithms regarding different tissues, organs and imaging modalities. Nowadays, skin melanoma is one of the most common serious malignancies in the human community. Consequently, automated and robust approaches have become an emerging need for accurate and fast clinical detection and diagnosis of skin cancer. Digital dermatoscopy is a clinically accepted device to register and to investigate suspicious regions in the skin. During the skin melanoma examination, mining the suspicious regions from dermoscopy images is generally demanded in order to make a clear diagnosis about skin diseases, mainly based on features of the region under analysis like border symmetry and regularity. Predominantly, the successful estimation of the skin cancer depends on the used computational techniques of image segmentation and analysis. In the current work, a social group optimization (SGO) supported automated tool was developed to examine skin melanoma in dermoscopy images. The proposed tool has two main steps, mainly the image pre-processing step using the Otsu/Kapur based thresholding technique and the image post-processing step using the level set/active contour based segmentation technique. The experimental work was conducted using three well-known dermoscopy image datasets. Similarity metrics were used to evaluate the clinical significance of the proposed tool such as Jaccard's coefficient, Dice's coefficient, false positive/negative rate, accuracy, sensitivity and specificity. The experimental findings suggest that the proposed tool achieved superior performance relatively to the ground truth images provided by a skin cancer physician. Generally, the proposed SGO based Kapur's thresholding technique combined with the level set based segmentation technique is very effective for identifying melanoma dermoscopy digital images with high sensitivity, specificity and accuracy.

Keywords: skin melanoma; social group optimization (SGO); Otsu; Kapur; level set; active contour

1. Introduction

Skin melanoma is one of the most critical widespread diseases that can affect people despite their race, gender and age, causing high mortality rates. Premature stage detection of melanoma can diminish these rates [1]. The skin melanoma commences in the interior regions as well as in associated skin segments. The accessibility of the latest therapeutic technologies will lead to early detection and

inspection of melanomas during routine pre-/post-screening processes. Once the dimension and the stage of melanoma are known, then physicians can plan the most suitable treatment procedure [2–5]. Typically, the melanoma screening practice involves the (i) visual examination of skin regions by a physician and the (ii) visual/computational evaluation by an experienced dermatologist. Most of the dermatologists examine the suspicious skin regions using the well-known ABCD (Asymmetry, Border, Color and Diameter) rule [6]. After confirming the skin cancer by visual inspection, the cancerous regions of skin are imaged by digital dermatoscopy for further investigation and definition of the treatment planning process. Digital dermoscopy images are generally colored RGB (red, green, blue) images that have been extensively adopted for automatic detection, boundary extraction and skin cancer investigation [7,8].

The automated analysis of skin cancer in dermoscopy images has inspired researchers to develop accurate computational techniques for such goal [9–17]. Xu et al. [18] proposed a boundary based segmentation of skin lesions for RGB skin images. Amelard et al. [9] discussed the intuitive feature mining from the Dermquest and Dermis image datasets. Silveira et al. [19] presented a detailed comparative analysis on various segmentation approaches for dermoscopy images of skin melanoma. This study suggests that the adaptive snake based segmentation combined with the expectation–maximization level set technique enhanced the segmentation results compared to the adaptive thresholding, gradient vector flow, level set method and fuzzy-based split-and-merge techniques. However, the analysis of melanoma in images is a very challenging task, particularly when the skin regions are disturbed by hair. The hair removal requires special image pre-processing approaches, which is time-consuming and may affect the quality of the original dermoscopic image. Hence, it is always recommended to have a simple and efficient automated procedure to analyze the acquired digital dermoscopy images with robustness against phase, dimension, color and orientation of the skin regions under analysis. Hence, in order to accomplish this goal, several image pre-processing procedures have been developed. For example, Lee et al. [20,21] proposed a computer based tool known as DullRazor to remove hair regions from skin cancer images. Wighton et al. [22] carried out an alternative approach for the DullRazor to eliminate the hair regions based on the inpainting technique. Mirzaalian et al. [23] proposed a filter to eliminate the same regions, and Satheesha et al. [24] suggested a pixel interpolation technique for the same purpose. Detailed surveys of existing hair regions removal and melanoma detection procedures are presented in [1,25].

Consequently, the main contribution of the present work is to propose an automated tool to mine cancerous regions from dermoscopy images. A two step (pre-processing and post-processing) approach was developed to mine the skin lesions. The pre-processing step is applied to enhance the melanoma region based on social group optimization (SGO) to support the Otsu's or Kapur's multi-level thresholding and image morphological operations. The post-processing step segments the enhanced melanoma using the level set or active contour approach. The Matlab software (Version 7, Release 14, License number 285705 with perpetual term, St. Joseph's College of Engineering, Chennai, India) was employed to implement the proposed tool. Well known melanoma image datasets, such as Dermis [26], Dermquest [26] and ISBI2016 challenge (hairy images) [27], were used. In order to evaluate the proposed tool, the mined image regions were compared against the ground truth (GT) provided by a physician. Consequently, the efficiency of the proposed melanoma image processing tool was confirmed using well-known similarity measures, including the Jaccard's index, Dice's coefficient, false negative rate and false positive rate. Statistical parameters, namely precision, F-measure, sensitivity, specificity, balanced classification rate, balanced error rate and accuracy, were also computed. Finally, the severity level of the detected skin melanoma was measured using the SkinCAD tool developed by Chang et al. [28].

2. Materials and Methods

The current work was devoted to the development of an automated tool for extracting infected skin regions from RGB dermoscopy images. The proposed tool integrates two main steps: the pre-processing and post-processing steps, described in the following.

2.1. Pre-Processing

The overall accuracy of the proposed tool depends mainly on the pre-processing step, which includes the SGO and Otsu or Kapur based multi-level thresholding that is followed by the application of the morphological procedure to improve the thresholded image.

2.1.1. Multi-Level Thresholding

Traditional and soft computing based multi-level thresholding techniques have great impact in engineering and medical fields [29–32]. In multi-level thresholding, a gray or RGB image is divided into different parts by relating similar pixels in order to trace and scrutinize significant information in the input image. The implementation of the thresholding process is essential to pre-process a raw image [33–35]. The Otsu and Kapur based image thresholding techniques have been extensively adopted by the researchers to threshold traditional and clinical images [36]. The Otsu based thresholding technique can provide the best threshold level for a given image by the maximization of the between-class variance function [37]. Several optimization techniques can be employed to support the multi-level thresholding. One of these optimization methods is the recently developed SGO algorithm. Since several studies have confirmed that the SGO algorithm achieved superior results compared to other existing meta-heuristic approaches [38,39], the current work carried out the SGO algorithm to optimize the levels of the applied multi-level thresholding.

2.1.2. Social Group Optimization

SGO is a soft computing procedure recently developed by Satapathy and Naik [38]. It has been developed by mimicking the behavior and knowledge transfer practice in human groups. The SGO algorithm includes two main steps, namely the (i) improving step, which synchronizes the positions of people (agents) based on the objective function, and the (ii) acquiring step that allows the agents to discover the best potential solution for the problem under concern. The mathematical model for the SGO is as follows [39].

Let us consider X_i as the initial knowledge of people in a group and $i = 1, 2, 3, \ldots, N$, with N as the total number of people in the group. If the optimization task needs a D-dimensional search space, then the knowledge term can be expressed as $X_i = (x_{i1}, x_{i2}, x_{i3}, \ldots x_{iD})$. For any problem, the fitness value can be defined as f_j, with $j = 1, 2, \ldots, N$. Thus, for the maximization problem, the fitness value can be written as:

$$Gbest_j = max\ \{f(X_i)\ for\ i = 1,2,\ldots N\} \quad (1)$$

In order to update the position (knowledge) of every individual in the group, the improving phase considers the following relation:

$$Xnew_{i,j} = c * Xold_{i,j} + R * (Gbest_j - Xold_{i,j}), \quad (2)$$

where *Xnew* is the new knowledge, *Xold* is the old knowledge, *Gbest* is the global best knowledge, R is a random numeral [0,1], and c represents the self-introspection parameter [0,1]. The value of c is chosen as 0.2 in [38,39], while, in the current work, the value of c was defined as 0.5 based on the trial and error approach.

During the acquiring phase, the agents will find the global solution based on knowledge updating process by randomly select one person from the group (X_r) based on $i \neq r$. Once the fitness value becomes $f(X_i) < f(X_r)$, then the following knowledge procedure is executed:

$$Xnew_{i,j} = Xold_{i,j} + R_a * (X_{i,j} - X_{r,j}) + R_b * (Gbest_j - X_{i,j}), \quad (3)$$

where R_a and R_b are random numbers having the range [0,1] and $X_{r,j}$ is the knowledge (position) value of the chosen individual. From Equations (2) and (3), it can be observed that the implementation of the SGO algorithm is simple compared to other algorithms existing in the image processing domain [40–48]. The steps of the standard SGO algorithm can be described as in Algorithm 1.

Algorithm 1: Standard Social Group Optimization Algorithm

Start

Assume five agents (i = 1,2,3,4,5)

Assign these agents to find the $Gbest_j$ in a D-dimensional search space

Randomly distribute the entire agents in the group throughout the search space during initialization process

Computethe fitness value based on the problem under concern

Updatethe orientation of agents using $Gbest_j = \max\{f(X_i)\}$

Initiatethe improving phase to update the knowledge of other agents in order to reach the $Gbest_j$

Initiatethe acquiring phase to further update the knowledge of agents by randomly choosing the agents with best fitness value

Repeatthe procedure till the entire agents move toward the best possible position in the D-dimensional search space

If all the agents have approximately similar fitness values ($Gbest_j$)

Then

Terminate the search and display the optimized result for the chosen problem

Else

Repeat the previous steps

End

Stop

The working principle of the SGO algorithm is illustrated in the flow diagram presented in Figure 1, where the blue agents are agents with $Gbest_j$.

In the present work, the SGO algorithm is considered to pre-process the input dermascopic image based on the Otsu's/Kapur's thresholding technique. The initial SGO parameters were assigned as follows: N was chosen as 20, i.e., the total number of people in the group was 20, D was assigned as three-dimensional space, c was fixed as equal to 0.5 denoting the self-introspection parameter and the number of iteration was set as 500.This optimization algorithm is used to find the optimal threshold value when using the Otsu/Kapur based thresholding technique during the segmentation process.

During the optimization search, the SGO algorithm adjusts randomly the thresholds of the input image and computes the J_{max} value of the Otsu/Kapur threholding technique. When J_{max} is reached, the SGO stops the search and provides the output image of the pre-processing step.

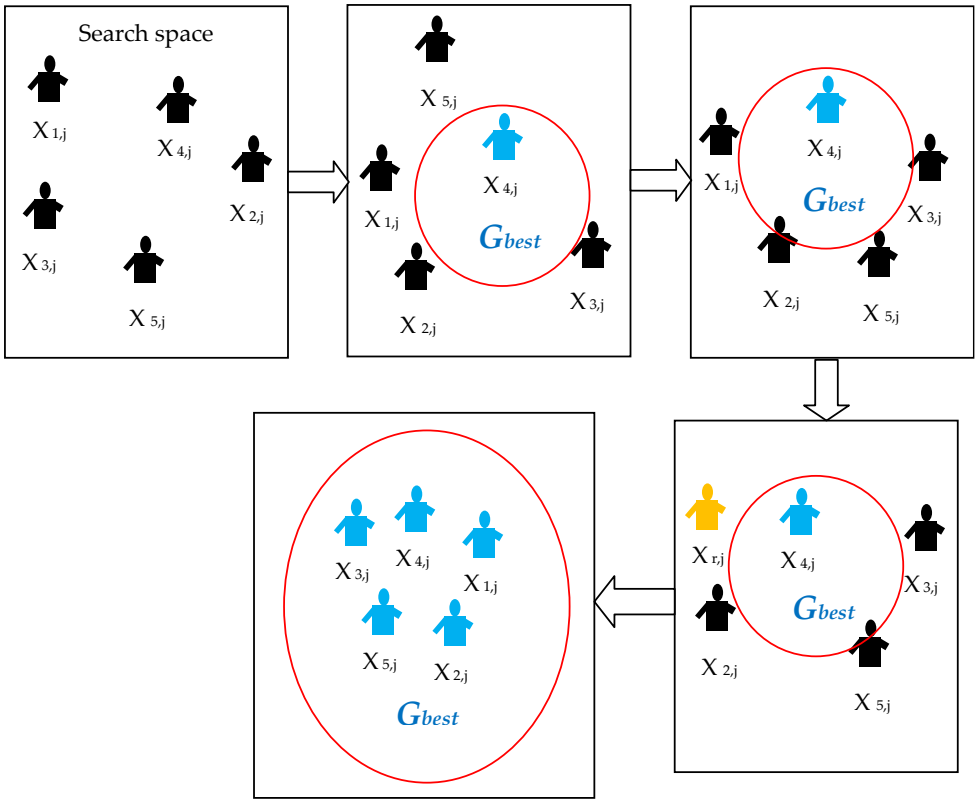

Figure 1. The working principle of the social group optimization (SGO) algorithm.

2.1.3. Otsu Based Thresholding

The Otsu based thresholding can provide the best threshold for a given image by maximizing the between-class variance function. Here, it is adopted for RGB image thresholding using the RGB histogram of the input image, which has a complex data size of [0, L-1]^3, where each color *R*, *G* and B has the range of [0, L-1]. Additionally, the SGO meta-heuristic algorithm is employed to formalize the meta-heuristic based segmentation procedure as follows [30,31].

In the range [0,1,2,…, L-1], assume *L* intensity levels with probability distribution P_o^E, which is given by:

$$p_o^E = \frac{h_o^E}{M} \quad \sum_{o=0}^{L-1} p_o^E = 1 \quad , \tag{4}$$

where *I* is a precise intensity level of range $\{0 \le o \le L-1\}$ for the color component *E* = {R,G,B}, *M* is the total number of image pixels, and h_o^E is the number of pixels for the analogous intensity level *O* in the component *C*. For each component, the total mean of the image is given by:

$$\mu_T^E = \sum_{i=0}^{L-1} op_o^E = 1 \quad . \tag{5}$$

The *m*-level thresholding procedure requires *m-1* threshold levels t_p^E, where *p* = 1,2,…,*m-1*, for a single color component R/G/B, and a similar process is repeated for other color components.

The image thresholding operation for a single color component is performed as:

$$F^E(w,h)=\begin{cases}0, & \\ \frac{1}{2}(t_1^E+t_2^E), & f^E(x,y)\le t_1^E \\ \vdots & t_1^E < f^E(x,y)\le t_2^E \\ \frac{1}{2}(t_{m-2}^E+t_{m-1}^E), & t_{m-2}^E < f^E(x,y)\le t_{m-1}^E \\ L-1, & f^E(x,y)> t_{m-1}^E \end{cases}, \quad \vdots \quad (6)$$

wherein h and w represent the height and width of the image with size $H \times W$. The probabilities of occurrence w_p^E of classes $D_p^E,\ldots,D_m^E$ are:

$$w_p^E=\begin{cases}\sum_{o=0}^{t_p^E} P_o^E, & p=1 \\ \sum_{o=t_p^E-1}^{t_p^E+1} P_o^E, & 1<p<m \\ \sum_{o=t_p^E-1}^{L-1+1} P_o^E, & p=m \end{cases}. \quad (7)$$

For each class, μ_p^E can be calculated using the following expression:

$$\mu_p^E=\begin{cases}\sum_{o=0}^{t_p^E} \frac{p_o^E}{w_p^E q}, & p=1 \\ \sum_{o=t_p^C-1}^{t_p^E+1} \frac{p_o^E}{w_p^E}, & 1<p<m \\ \sum_{o=t_p^E-1}^{L-1+1} \frac{p_o^E}{w_p^E}, & p=m \end{cases}. \quad (8)$$

Finally, the Otsu's between-class variance components are obtained as:

$$\sigma_B^{E^2} = \sum_{p=1}^{m} w_p^E\left(\mu_p^E-\mu_T^E\right)^2, \quad (9)$$

where w_p^E is the occurrence probability. The m-level thresholding is summarized to an optimization problem in order to find the optimal threshold value that maximizes the fitness (J_{max}) of each image component E = {R,G,B} defined as:

$$J_{max}=\max_{1<t_o^E<,\cdots,L-1}\sigma_B^{E^2}(t_p^E). \quad (10)$$

Here, a tri-level image thresholding procedure was implemented to pre-process the image under analysis based on the recent work by Rajinikanth et al. [8]. The tri-level approach enhances the input image effectively and the pre-processed image is then considered for the segmentation task.

2.1.4. Kapur Based Thresholding

The Kapur based segmentation technique has been initially proposed for segmenting gray scale images using the histogram entropy [49]. The proposed technique determines the optimal Th that maximizes the overall entropy [50–53]. Thus, for the image thresholds vector $Th = [t_1, t_2, \ldots, t_{k-1}]$, the Kapur's entropy is given by:

$$J_{max}=f_{Kapur}(Th)=\sum_{p=1}^{k}H_j^C, \quad (11)$$

where C = {R,G,B}, for the three components. Typically, the entropy of each component is calculated independently based on the chosen threshold t value. For tri-level thresholding, the entropy can be given by:

$$\begin{aligned} H_1^E &= \sum_{p=1}^{t_1} \frac{Ph_p^E}{\omega_0^E} ln\left(\frac{Ph_p^E}{\omega_0^E}\right), \\ H_2^E &= \sum_{j=t_{l+1}}^{t_2} \frac{Ph_p^E}{\omega_1^E} ln\left(\frac{Ph_p^E}{\omega_1^E}\right), \\ H_3^E &\sum_{p=t_{2+1}}^{L} \frac{Ph_p^E}{\omega_2^E} ln\left(\frac{Ph_p^E}{\omega_2^E}\right) \end{aligned} \quad , \tag{12}$$

where Ph_p^E is the intensity levels' probability distribution and $\omega_0^E, \omega_1^E, .. \omega_{k-1}^E$ the occurrence probability for k levels. Detailed descriptions about the Kapur based thresholding technique are presented in [52,53], and an implementation is described in [51].

2.1.5. Image Morphology

In image processing, morphological operations are generally used to improve the visual appearance of input images. Usually, the quality and the appearance of skin melanoma images are poor due to several factors such as multiple colors, irregular shapes and associated hair regions. Hence, in this work, morphological operations, such as line based structuring element (*strel*) and image fill (*imfill*), were used to enhance the edges and appearance of the pre-processed skin melanoma images. This morphological procedure enhances the suspicious regions of the thresholded images and guarantees faster segmentations during the post-processing step.

2.2. Post-Processing

The post-processing step is implemented to extract the abnormal regions from the pre-processed dermoscopy images. In the current work, the well-known level set and active contour segmentation approaches were independently studied and their results compared in terms of segmentation accuracy, speed and complexity.

2.2.1. Level Set

Level set (LS) approach has been broadly used in image segmentation problems as, for example, in the ones described in [54,55]. Here, the advantage of the LS technique was taken into account to enhance the active contour approach, since the LS technique can produce contours of complex topology able to handle split and merge operations that can occurduring the image segmentation process. The recent version of the LS technique suggested in [56] was implemented in the proposed tool, the curve evolution being given by:

$$BZ = \frac{\partial \varepsilon(s,t)}{\partial t} \quad , \tag{13}$$

with ε denoting the curve vector with spatial parameter s and temporal variable t, B the speed function and Z the inmost curve normal vector ε. The curve evolution given by Equation (13) can be converted into the LS technique using the dynamic contour $\varepsilon(s,t)$ as the zero of a time charged level set function $\phi(x,y,t)$. The LS function is then used to track the similar pixel group in a pre-processed image based on its boundary. The function ϕ generates positive values outside the zero level contour and negative values inside. The inner most normal vector Z can be given as:

$$Z = \frac{-\nabla \phi}{\nabla \phi} \quad , \tag{14}$$

where ∇ represents the gradient operator. Thus, the LS evolution can be expressed as:

$$\frac{\partial \phi}{\partial t} = B|\nabla \phi| \quad (15)$$

More details regarding the used LS function can be found in [57].

2.2.2. Active Contour

Active contour (AC) is an essential segmentation procedure to extract suspicious region from a pre-processed image. Here, the deformable snake based global active contour (GAC) [58] and the localized active contour (LAC) [59] were used to extract the suspicious region from the pre-processed image. This procedure has two essential steps, namely the initialization, and the boundary detection and extraction based on energy minimization. This approach tracks the similar pixel groups existing in a pre-processed input image based on an energy minimization concept [60].The energy function of the active contour can be described as:

$$\theta_{GAC}(U) = \int_0^{L(U)} g(|\nabla I_0 U(s))| \, ds \quad (16)$$

where ds is the Euclidean component of the contour length and $L(U)$ is the length of curve U, which satisfies $L(U) = \int_0^{L(U)} ds$. The parameter g is an edge indicator, which can be defined as:

$$g(|\nabla I_0|) = \frac{1}{1 + \beta |\nabla I_0|^2} \quad (17)$$

where β is an arbitrary constant and I_0 represents the input image. The energy value decreases rapidly based on the edge value, which is based on the gradient descent criterion. This procedure is mathematically represented as:

$$\partial_t U = (kg - \langle \nabla_g, Q \rangle) Q \quad (18)$$

where $\partial_t U = \partial U / \partial t$ represents the deformation in the snake model and t is the iteration time. The normal and curvature of the snake U are Q and k, respectively. In this procedure, the snake silhouette is continuously corrected until the minimal value of the energy θ_{GAC} is reached.

During the post-processing operation, the level set and the active contour segmentation techniques were separately used to extract the abnormal skin region from the SGO assisted Otsu/Kapur based pre-processed image. In order to confirm the segmentation accuracy, a comparative evaluation between the level set and the active contour based segmentation results was performed.

2.3. Implementation of the Proposed Tool

The implementation of the proposed pre-processing and post-processing approach is presented here. Initially, the Otsu based thresholding technique combined with the level set segmentation technique is discussed. Then, considerations are presented concerning the Kapur based thresholding technique.

The implementation of the Otsu based thresholding technique combined with the level set segmentation technique can be summarized as:

Step 1: Initialize the SGO algorithm with the initial algorithm parameters and using the Otsu tri-level pre-processing based approach;

Step 2: Arbitrarily, adjust the *R*, *G*, and *B* channel threshold values until the between class variance is maximized (J_{max}). When the optimal thresholds are reached, finish the heuristic search and record the pre-processed image;

Step 3: Perform morphological operations in order to improve the pre-processed image;

Step 4: Initiate the post-processing technique in order to extract the abnormal skin region using the level set based segmentation technique;

Step 5: After extracting the region of interest, a comparative analysis is performed between the ground truth and the extracted skin region using well known image quality and similarity measures;

Step 6: By considering the segmented region, the severity of the skin cancer is further examined with the SkinCAD tool and the performance value is recorder.

A similar procedure was adopted concerning the Kapur based thresholding technique combined with the other segmentation procedures considered in this article: the active contour segmentation technique. Finally, a detailed comparative analysis between the results obtained by the level set and the active contour based approaches was performed in order to choose the appropriate image processing approaches to examine the skin cancer dataset.

2.4. Image Quality Assessment

During the extracted lesion and ground truth comparison process, the image similarity measurements, like Jaccard Index (*JI*), Dice Coefficient (*DC*), false negative rate (*FNR*) and false positive rate (*FPR*) were calculated [61] using the following mathematical expressions:

$$JI(I_{gt}, I_t) = I_{gt} \cap I_t / I_{gt} \cup I_t \,, \tag{19}$$

$$DC(I_{gt}, I_t) = 2\left(I_{gt} \cap I_t\right) \Big/ \left|I_{gt}\right| \cup \left|I_t\right| \,, \tag{20}$$

$$FPR(I_{gt}, I_t) = \left(I_{gt} / I_t\right) \Big/ (I_{gt} \cup I_t) \,, \tag{21}$$

$$FNR(I_{gt}, I_t) = \left(I_t / I_{gt}\right) \Big/ (I_{gt} \cup I_t) \,, \tag{22}$$

where I_{gt} represents the corresponding ground truth, I_t stands for the extracted lesion, $\cup$ is the union operation and $\cap$ is the intersection operation. Furthermore, the image statistical metrics precision (*PRE*), F-measure (*FM*), sensitivity (*SEN*), specificity (*SPE*), balanced classification rate (*BCR*), balanced error rate (*BER*) and accuracy (*ACC*), were also computed [62–66] using the following mathematical expressions:

$$\begin{gathered} PRE = TP/(TP + FP), \\ FM = 2\ TP/(2\ TP + FP + FN), \\ SEN = TP/(TP + FN), \\ SPE = TN/(TN + FP), \\ BCR = 1/2\ (TP/(TP + FN) + TN/(TN + FP)), \\ BER = 1\ -\ BCR, \\ ACC = (TP + TN)/(TP + TN + FP + FN), \end{gathered} \tag{23}$$

where *TP*, *TN*, *FP* and *FN* denote the true positive, true negative, false positive and false negative, respectively.

2.5. Proposed Tool

The aforementioned methodologies were used in the current work to segment and analyze dermoscopy images as depicted in Figure 2.

Figure 2 depicted that initially the SGO assisted Otsu/Kapur based tri-level thresholding is performed on the RGB input image in order to group the similar pixels as healthy skin, lightly spread lesion and acutely spread lesion. In order to group the pixels of the light and deep lesions, the thresholded RGB image is transformed into a gray scale image and a morphological procedure is

applied to smooth the separated skin regions. Later, the grouped area of light and deep lesions is extracted using the level set/active contour based segmentation approach. Finally, the extracted melanoma region is compared against the corresponding ground truth to validate the ability of the proposed computational tool.

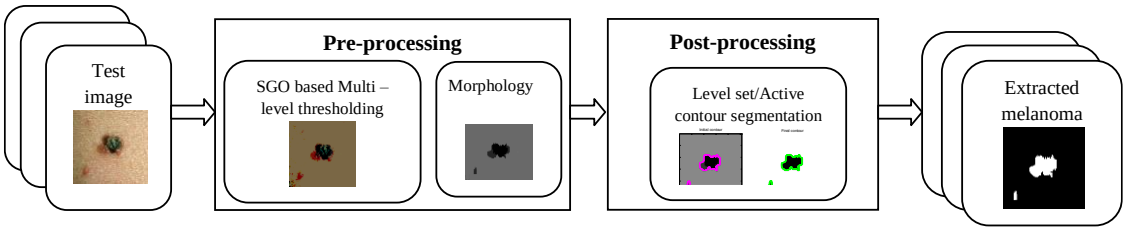

Figure 2. The proposed computational tool to examine skin abnormality in dermoscopy images.

In addition, analysis using the SkinCAD tool, which is a computer aided diagnosis tool for digital dermoscopy images developed by Chang et al. [28], was performed. This tool supports inbuilt facilities to analyze both melanocytic and non-melanocytic skin lesions based on shape, texture and color features. By using this tool, it is easy to extract the complete information of RGB skin melanoma images in order to analyze the probability and risk of lesion malignancy based on the Asymmetry (A), Border (B), Color (C) and Diameter (D) criteria, which are defined by the well-known ABCD rule. This tool initially extracts the suspicious region of the input dermoscopy image based on a pattern matching concept. During this process, the input image is compared against a mask image. The mask can be manually generated using the skinCAD or obtained using another image processing technique. Chang et al. reported better values of sensitivity (85.63%), specificity (87.65%) and accuracy (90.64%) using manually generated masks. These values can be enhanced by using masks obtained using the most recent image segmentation procedures. Consequently, the current proposed approach was compared to the solution developed by Chang et al. in order to prove its efficiency.

The Matlab 7 software was used to implement the proposed approach. In order to test the developed tool, melanoma images existing in Dermis (44 images), Dermquest (76 images) and ISBI2016 challenge (20 images) were used. All these melanoma image datasets are provided with the corresponding ground truth images provided by an expert. Initially, the test images as well as the ground truth images of Dermis and Dermquest image databases were resized to 256 × 256 pixels. From the ISBI2016 challenge dataset, the most complex images, i.e., the dermoscopy images with hair, were used in their original size.

3. Results and Discussion

In the present work, the SGO algorithm is employed to select the optimal threshold values of the Otsu/Kapur based multi-level thresholding technique. Compared with other existing algorithms in the literature, the SGO algorithm is very simple in terms of implementation, since it only requires few initial parameters, namely the iteration value, the number of agents and the self-introspection value 'c'. In the previous works regarding the SGO algorithm, a value of 0.2 for the parameter c [29,30] was suggested, but, here, a trial and error procedure was performed and the value that offered the best convergence rate along with the optimized result was found to be 0.5. The experimental study also confirmed that the proposed SGO algorithm offered better execution time compared to other well-known heuristic algorithms such as PSO [52], FA [42,47] and BA [41] based thresholding procedures. Examples of the used RGB images are presented in Figure 3 along with the corresponding histogram of the three channels (i.e., R, G and B components) and the associated ground truth.

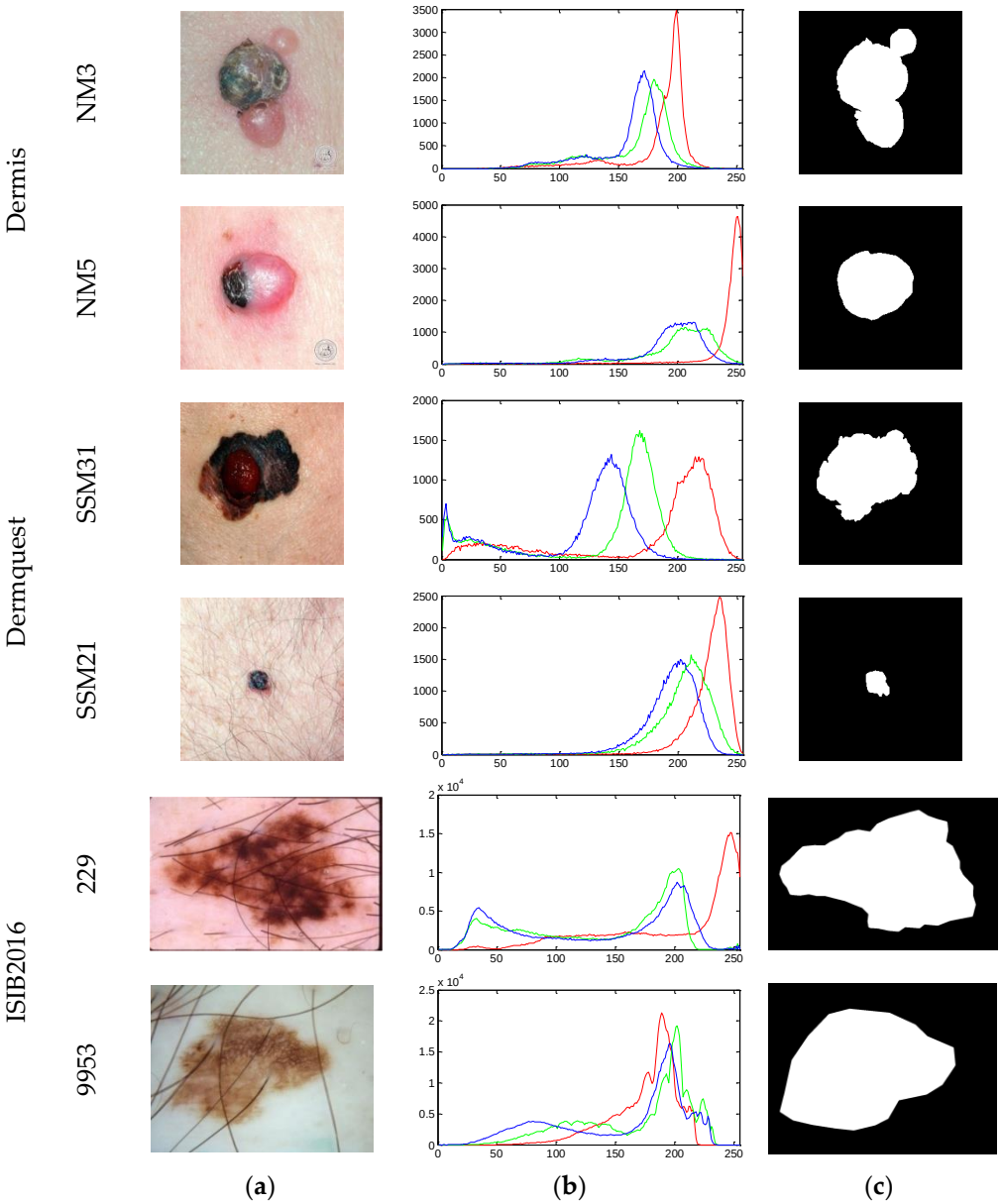

Figure 3. Sample test images from the chosen skin cancer image dataset: (**a**) test images; (**b**) RGB histograms (x- axis represents the threshold distribution and y-axis denotes the pixel distribution) and (**c**) corresponding ground truths of the images.

Previous works from the literature confirm that finding the optimal threshold value for a RGB input image is more complex comparatively to the corresponding gray scale image due to its complex and nonlinear histograms. In order to find the optimal threshold for a color image, it is necessary to examine the *R*, *G*, and *B* channels separately by a suitable pre-processing approach. Here, the SGO algorithm combined with the Otsu based thresholding technique is used to identify the optimal threshold for the image under analysis and the corresponding outputs are recorded. Then, a similar pre-processing procedure is repeated with the SGO algorithm combined with the Kapur based thresholding technique and the outcomes are recorded. The overall quality of the proposed image processing tool relies on the pre-processing approach. Hence, an attempt was made to examine the performance of the Otsu and Kapur based thresholding techniques widely used in the image processing community to pre-process input images [47–53].

Figure 4 illustrates the obtained results of the proposed optimized Otsu and level set based segmentation approach when applied to the test images. Initially, the proposed SGO based Otsu based tri-level thresholding procedure is performed on the sample images; results of these steps were

presented in the second column of Figure 4. Considering the obtained results for image NM3, it can be reported that at the end of the SGO based Otsu search, the SGO continuously explores the RGB histograms until the between class values is maximized. At the end, the search offers the optimized thresholds, such as *R* [52, 187, 224], *G* [74, 147, 206] and *B* [39, 170, 231]. This search also offered a maximized Otsu's between class variance value of 2107.85 [47]. From a visual assessment of the original NM3 test image and the thresholded image, it is observed that the thresholding process enhance the melanoma region based on pixel grouping concept. This image is then further processed using the morphological procedure discussed in Section 2. After completing the pre-processing task, the well-known segmentation procedures based on level set, global active contour and local active contour were applied to mine the region of interest from the dermoscopy image and their results compared.

With the intention of evaluating the proposed approach superiority, complex dermoscopic images, mainly images with hair, such as SSM21, 229 and 9953, were studied. The results in Figure 4 suggest that the proposed pre-processing approach is very efficient in eliminating the hair regions from the input images and can be used as an interesting alternative to the existing hair removing procedures [20,22–25].

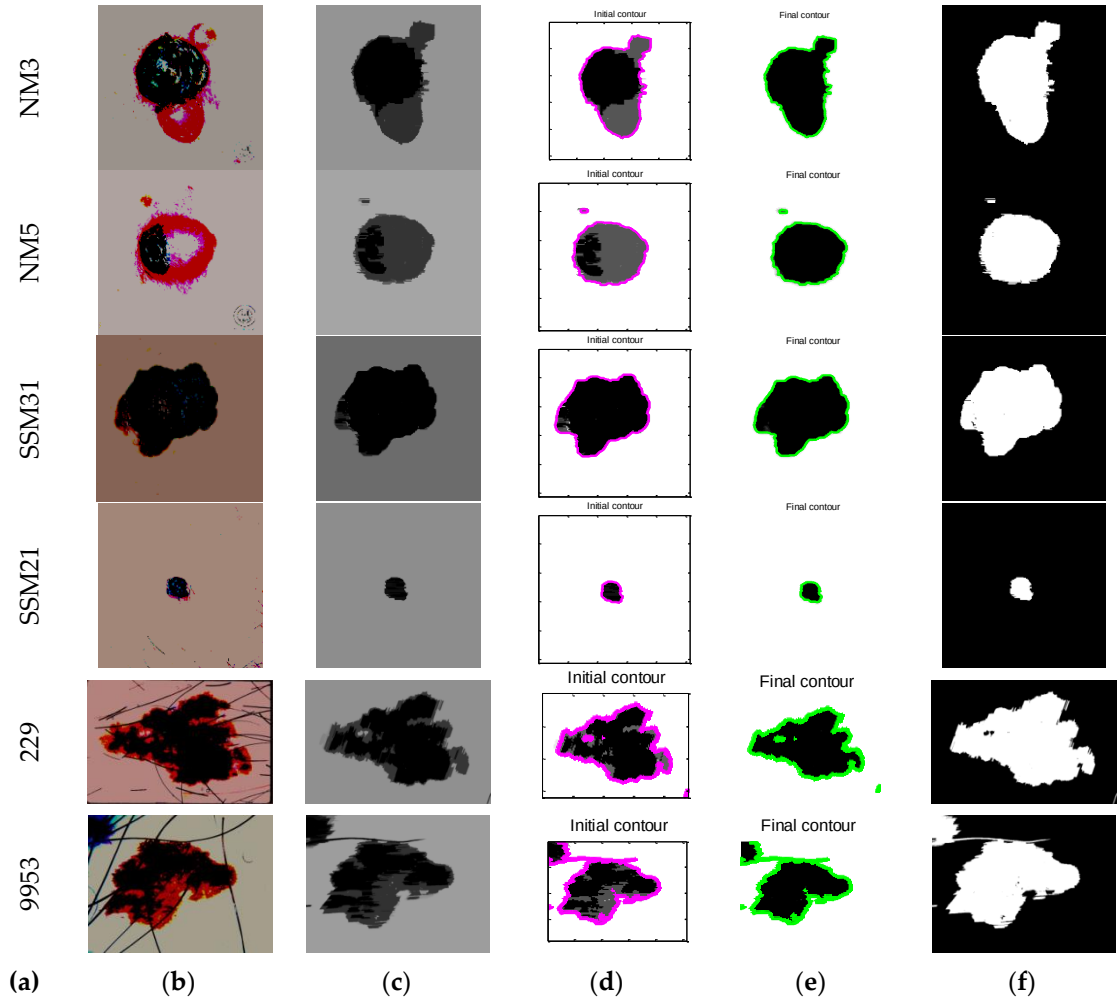

Figure 4. Results obtained with Otsu and level set based segmentation approaches: (**a**) Pseudo name of image as in database; (**b**) output of the tri-level thresholding technique; (**c**) output of the morphological procedure; (**d**) initial contour of the level set segmentation; (**e**) final contour of the level set segmentation; and (**f**) extracted region.

Afterwards, the performance of well-known active contour approaches, such as the GAC and LAC, were tested on the SGO based Otsu pre-processed images, Figure 5.

(**a**) GAC (**b**) Extracted region (**c**) LAC (**d**) Extracted region

Figure 5. Active contour based segmentation results for the sample image with pseudo name NM3: (**a**,**b**) are the results of the (global active contour) GAC, while (**c**,**d**) are the results of the (localized active contour) LAC.

Along with Figure 5, the results demonstrated that the total required run time by the LAC is quite large compared to the GAC. Moreover, these active contour approaches require a seed initialization procedure in order to begin the segmentation task, whereas the level set is an automated approach that does not require any initialization. Afterwards, image similarity metrics and statistical metrics were computed to evaluate the LS, GAC and LAC performance by comparing the extracted melanoma regions with the corresponding found truths existing in the test datasets. Tables 1 and 2 report the image similarity indices and image statistical measures, respectively, which were computed from the segmentation results obtained using the proposed SGO based Otsu and the LS/GAC/LAC.

The results in Tables 1 and 2 indicated that the proposed approach is very efficient in analyzing the melanomas from the dermoscopic image datasets. It can be established that, for most of the image cases, the LS based segmentation procedure offered better results than the GAC and LAC. Afterwards, the proposed segmentation approach was then repeated for the used image datasets with SGO based Kapur based threshold, Figure 6.

Figure 6 suggests that the LS and GAC provides superior results compared to LAC. This finding is confirmed by the values indicated in Table 3.

Table 1. Image similarity measure of SGO based Otsu pre-processing procedure. *JI*: Jaccard Index; *DC*: Dice Coefficient; *FPR*: false positive rate; *FNR*: false negative rate; LS: level set.

Image	Segmentation Approach	*JI*	*DC*	*FPR*	*FNR*
NM3	LS	0.8794	0.9305	0.1285	0.0101
	GAC	0.8728	0.9310	0.1004	0.0073
	LAC	0.8744	0.9311	0.1026	0.0193
NM5	LS	0.8395	0.9004	0.0885	0.0064
	GAC	0.8226	0.8917	0.1743	0.0110
	LAC	0.8106	0.8853	0.1006	0.0097
SSM31	LS	0.8652	0.9106	0.0713	0.0093
	GAC	0.8408	0.9274	0.0945	0.0115
	LAC	0.8511	0.9037	0.0836	0.0284
SSM21	LS	0.8316	0.8925	0.0814	0.0377
	GAC	0.8014	0.8818	0.1004	0.0604
	LAC	0.8028	0.8674	0.0560	0.0840
229	LS	0.8284	0.8911	0.0106	0.0947
	GAC	0.8004	0.8972	0.0219	0.0956
	LAC	0.8084	0.8779	0.0724	0.0821
9953	LS	0.7827	0.8922	0.0084	0.0726
	GAC	0.8173	0.9105	0.0202	0.0622
	LAC	0.8091	0.9007	0.0115	0.0519

Table 2. Image statistical values of SGO based Otsu pre-processing procedure.*PRE*: precision; *FM*: F-measure; *SEN*: sensitivity; *SPE*: specificity; *BCR*: balanced classification rate; *BER*: balanced error rate; *ACC*: accuracy.

Image	Approach	*PRE*	*FM*	*SEN*	*SPE*	*BCR*	*BER%*	*ACC*
NM3	LS	0.9981	0.9813	0.9652	0.9939	0.9793	2.0606	0.9792
	GAC	0.9941	0.9852	0.9765	0.9799	0.9782	2.1781	0.9782
	LAC	0.9930	0.9843	0.9758	0.9759	0.9759	2.4114	0.9759
NM5	LS	0.9980	0.9911	0.9844	0.9888	0.9866	1.3403	0.9866
	GAC	0.9998	0.9774	0.9561	0.9990	0.9775	2.2420	0.9773
	LAC	0.9998	0.9789	0.9589	0.9992	0.9791	2.0882	0.9789
SSM31	LS	0.9988	0.9847	0.9709	0.9964	0.9837	1.6268	0.9836
	GAC	0.9986	0.9822	0.9663	0.9957	0.9810	1.8980	0.9809
	LAC	0.9993	0.9825	0.9662	0.9980	0.9821	1.7858	0.9820
SSM21	LS	0.9975	0.9983	0.9990	0.8585	0.9288	7.1187	0.9261
	GAC	0.9966	0.9978	0.9990	0.8087	0.9038	9.6129	0.8988
	LAC	0.9968	0.9979	0.9991	0.8194	0.9092	9.0752	0.9048
229	LS	0.8629	0.9261	0.9993	0.7867	0.8930	10.6964	0.8866
	GAC	0.9641	0.9703	0.9767	0.9511	0.9639	3.6049	0.9638
	LAC	0.9646	0.9723	0.9802	0.9517	0.9659	3.4019	0.9658
9953	LS	0.8465	0.8967	0.9531	0.7139	0.8335	16.6418	0.8249
	GAC	0.8946	0.9436	0.9982	0.8053	0.9018	9.8166	0.8966
	LAC	0.8919	0.9424	0.9990	0.7996	0.8993	10.0619	0.8938

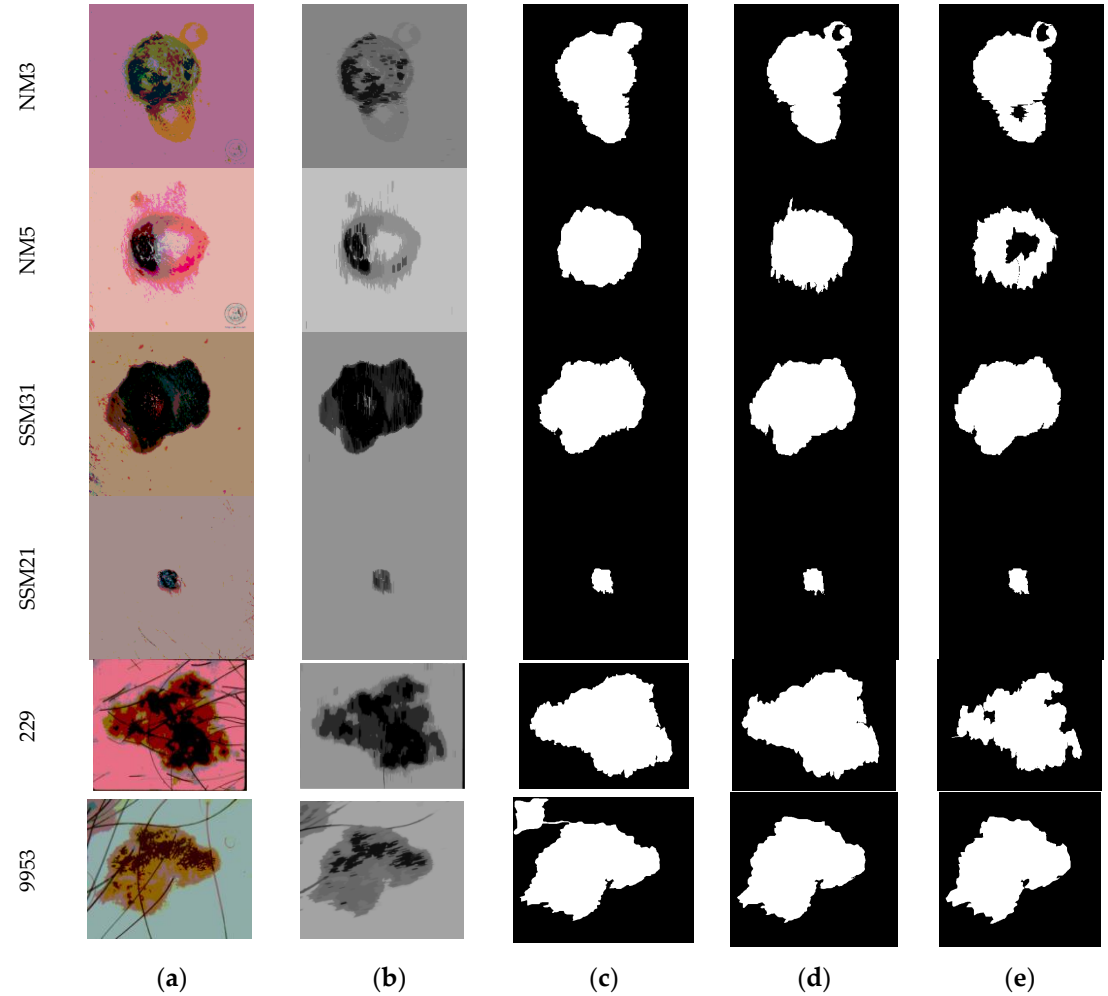

Figure 6. Outcomes of the Kapur based thresholding approach: (**a**) tri-level thresholding; (**b**) morphological procedure; (**c**) extracted region using LS; (**d**) extracted region using GAC; and (**e**) extracted region using LAC.

The values in Table 3 indicate that the *JI*, *DC*, *FPR* and *FNR* values obtained with the SGO based Kapur and LS are better than the ones obtained with the SGO based Kapur and GAC or SGO based Kapur and LAC. Additionally, the overall average results for all the (44 + 76 + 20) 140 test images are reported in Tables 4 and 5 regarding the average values of the image similarity indexes, including *JI*, *DC*, *FPR* and *FNR*, and the statistical indexes, such as *PRE*, *FM*, *SEN*, *SPE*, *BCR*, *NER* and *ACC*.

Table 3. Image similarity measures concerning the Kapur based pre-processing procedure.

Image	Segmentation Approach	*JI*	*DC*	*FPR*	*FNR*
NM3	LS	0.8852	0.9391	0.1225	0.0064
	GAC	0.8669	0.9287	0.1174	0.0312
	LAC	0.8401	0.9131	0.1079	0.0692
NM5	LS	0.8111	0.8957	0.2320	7.10×10^{-4}
	GAC	0.8004	0.8891	0.2482	9.13×10^{-4}
	LAC	0.6695	0.8020	0.2226	0.1815
SSM31	LS	0.9102	0.9530	0.0948	0.0035
	GAC	0.8971	0.9458	0.1099	0.0043
	LAC	0.8989	0.9468	0.1102	0.0020
SSM21	LS	0.8157	0.8985	0.0525	0.1415
	GAC	0.7792	0.8759	0.0516	0.1806
	LAC	0.7658	0.8674	0.0560	0.1913
229	LS	0.8031	0.8908	0.0029	0.1946
	GAC	0.7985	0.8879	0.0015	0.2003
	LAC	0.7355	0.8476	0.0908	0.1977
9953	LS	0.7253	0.8408	0.0000	0.2747
	GAC	0.9271	0.9622	0.0266	0.0483
	LAC	0.9223	0.9596	0.0313	0.0488

Table 4. Overall results for the image similarity metrics with the proposed approach.

Approach		Value	*JI*	*DC*	*FPR*	*FNR*
Otsu based threshold	LS	Min	0.6924	0.7216	0.0048	0.0035
		Max	0.8917	0.9506	0.1281	0.1016
		Average	0.8217	0.8812	0.0725	0.0883
	GAC	Min	0.5729	0.7104	0.0051	0.0052
		Max	0.8611	0.9422	0.1316	0.1218
		Average	0.8016	0.8961	0.0857	0.0829
	LAC	Min	0.5748	0.7048	0.0033	0.0029
		Max	0.8573	0.9518	0.1725	0.1314
		Average	0.8005	0.8873	0.0815	0.0528
Kapur based threshold	LS	Min	0.6284	0.6826	0.0051	3.41×10^{-4}
		Max	0.9165	0.9517	0.1177	0.2818
		Average	0.8296	0.8832	0.0615	0.0726
	GAC	Min	0.5477	0.7062	0.0038	5.72×10^{-4}
		Max	0.8917	0.9415	0.1226	0.2661
		Average	0.8188	0.9004	0.0744	0.0779
	LAC	Min	0.5385	0.6863	0.0028	4.08×10^{-4}
		Max	0.8618	0.9571	0.1534	0.2514
		Average	0.8192	0.8916	0.0795	0.0528

Table 5. Overall results for the image statistical metrics with the proposed approach.

Approach		*PRE*	*FM*	*SEN*	*SPE*	*BCR*	*BER%*	*ACC*
Otsu based threshold	LS	0.9812	0.9795	0.9827	0.9014	0.9331	5.7715	0.9517
	GAC	0.9796	0.9727	0.9803	0.8958	0.9186	6.0843	0.9416
	LAC	0.9685	0.9736	0.9774	0.8971	0.9158	5.8025	0.9481
Kapur based threshold	LS	0.9826	0.9805	0.9841	0.9116	0.9284	4.9963	0.9619
	GAC	0.9803	0.9772	0.9825	0.9028	0.9188	5.8670	0.9571
	LAC	0.9715	0.9758	0.9781	0.8987	0.9172	5.7016	0.9486

The overall average results reported in Tables 4 and 5prove that the average values of the image similarity indexes and of the statistical indexes, respectively, are better by using the SGO based Kapur and LS approach compared to the other procedures considered in this study. Generally, the proposed approach using SGO based Kapur supports the image pre-processing and LS segmentation more efficiently in order to extract the skin lesions both from simple and complex dermoscopic images comparatively to the other studied alternatives. The results of Table 5 indicate that this approach offers superior sensitivity of98.41%, specificity of91.16% and accuracy of 96.19% on the used image datasets. Furthermore, the classification and detection accuracy of the SGO based Otsu and LS as well as SGO based Kapur and LS were tested using the *skinCAD* tool [28]. The corresponding results are illustrated in Figure 7 and indicated in Table 6.

(**a**) (**b**) (**c**) (**d**)

Figure 7. Prediction of melanoma severity in image NM3 using SkinCAD: (**a**) test image; (**b**) extracted melanoma region; (**c**) initial trace; and (**d**) final trace.

Table 6. Results obtained with SkinCAD tool.

Image	Segmentation Approach	Lesion Malignancy			
		Otsu		Kapur	
		Probability	Risk	Probability	Risk
NM3	LS	0.8363	High	0.8784	High
	GAC	0.7947		0.8216	
	LAC	0.8144		0.8027	
NM5	LS	0.8153		0.8639	
	GAC	0.8271		0.8406	
	LAC	0.8026		0.8013	
SSM31	LS	0.8246		0.8815	
	GAC	0.8116		0.8217	
	LAC	0.8075		0.8015	
SSM21	LS	0.7260		0.8037	
	GAC	0.7826		0.8110	
	LAC	0.7624		0.8046	
229	LS	0.8016		0.8218	
	GAC	0.8261		0.8639	
	LAC	0.8136		0.7915	
9953	LS	0.7940		0.8125	
	GAC	0.8003		0.8016	
	LAC	0.8117		0.7918	

The *skinCAD* tool compares the input test image (Figure 7a) and the mask (Figure 7b) to create the initial and final trace as shown in Figure7c,d. After creating the final trace, the *skinCAD* tool considers the inner region of the trace and applies the ABCD rule as discussed previously. The tool

analyzes the traced region with various features along with image similarity measures and statistical measures and provides the probability of lesion malignancy and the risk rate. Based on the probability as well as the risk rates, the suitable treatment procedure can be planned during routine clinical examination.

Consequently, it can be suggested that if the proposed approach is combined with the *skinCAD* tool, then the sensitivity, specificity and accuracy of the skin melanoma discovery practice can be improved and skin lesions can be efficiently diagnosed irrespective of the image complexities. Thus, the proposed approach can be considered to analyze routine clinical skin melanoma images based on the comparative analysis that is carried out between the Otsu and Kapur threshold techniques based on the SGO algorithm.

4. Conclusions

In the current work, a novel tool was proposed to extract suspicious region from RGB dermoscopic images. This tool included a two steps procedure with SGO based Otsu/Kspur tri-level based thresholding as the pre-processing stage and level set/active contour based segmentation as the post-processing stage. In order to test the proposed computational tool, three well-known skin melanoma datasets, namely Dermis (44 images), Dermquest (76 images) and ISBI2016 challenge (20 images), were used. Initially, the SGO based Otsu and LS approach was implemented and then the proposed approach was also used with the prominent active contour approaches, namely GAC and LAC. Similar experiments were performed with the SGO based Kapur.

The performances of Otsu/Kapur as well as LS/GAC/LAC were assessed using well-known image similarity metrics and images statistical metrics. The results confirmed that the proposed tool is very effective in extracting lesion sections from hairy skin images. The comparative study performed between the extracted melanoma regions and the corresponding ground truths confirmed that the SGO based Kapur and LS based approach achieved superior results compared to the alternatives studied in the present study. Finally, the detection accuracy of the proposed tool was validated using the *skinCAD* tool and the probabilities of the lesion malignancy and the risk factors were obtained.

From the experimental results, it could be established that the proposed SGO based Kapur and LS based approach is very efficient in extracting melanoma regions from digital dermoscopic images with high values of sensitivity, specificity and accuracy.

In the near future, the proposed tool should be further evaluated using larger image datasets, including dermoscopic images acquired in real medical scenarios. On the other hand, additionally to the ABCD rule, other assessment rules, like the 7-point checklist and Menzies' method, should be studied.

Acknowledgments: João Manuel R. S. Tavares gratefully acknowledges the funding of Project NORTE-01-0145-FEDER-000022 - SciTech—Science and Technology for Competitive and Sustainable Industries, cofinanced by "Programa Operacional Regional do Norte" (NORTE2020), through "Fundo Europeu de Desenvolvimento Regional" (FEDER).

Author Contributions: Nilanjan Dey and João Manuel R. S. Tavares conducted the study design; Experimental work: Nilanjan Dey, Venkatesan Rajinikanth and Amira S. Ashour completed the experimental work; Results analysis and manuscript preparation were conducted by all authors; and manuscript proof and submission were completed by Nilanjan Dey and João Manuel R. S. Tavares.

Conflicts of Interest: The authors declare no conflict of interest.

References

1. Premaladha, J.; Sujitha, S.; Priya, M.L.; Rajichandran, K.S. A survey on melanoma diagnosis using image processing and soft computing techniques. *Res. J. Inf. Tech.* **2014**, *6*, 65–80.
2. Celebi, M.E.; Zornberg, A. Automated quantification of clinically significant colors in dermoscopy images and its application to skin lesion classification. *IEEE Syst. J.* **2014**, *8*, 980–984.
3. Celebi, M.E.; Iyatomi, H.; Schaefer, G.; Stoecker, W.V. Lesion border detection in dermoscopy images. *Comput. Med. Imag. Graph.* **2009**, *33*, 148–153.

4. Celebi, M.E.; Kingravi, H.; Uddin, B.; Iyatomi, H.; Aslandogan, A.; Stoecker, W.V.; Moss, R.H. A methodological approach to the classification of dermoscopy images. *Comput. Med. Imag. Graph.* **2007**, *31*, 362–373.
5. Amelard, R.; Glaister, J.; Wong, A.; Clausi, D.A. Melanoma decision support using lighting-corrected intuitive feature models, *Comput. Vis. Tech. Diagn. Skin Cancer* **2013**, 193–219.
6. Nachbar, F.; Stolz, W.; Merckle, T.; Cognetta, A.B.; Vogt, T.; Landthaler, M.; Bilek, P.; Braun-Falco, O.; Plewig, G. The ABCD rule of dermatoscopy: High prospective value in the diagnosis of doubtful melanocytic skin lesions. *J. Am. Acad. Dermatol.* **1994**, *30*, 551–559.
7. Barata, C.; Celebi, M.E.; and Marques, J.S. Improving dermoscopy image classification using color constancy. *IEEE J. Biomed. Health. Inform.* **2015**, *19*, 1146–1152.
8. Rajinikanth, V.; Raja, N.S.M.; Satapathy, S.C.; Fernandes, S.L. Otsu's multi-thresholding and active contour snake model to segment dermoscopy images. *J. Med. Imag. Health Inf.* **2017**, *7*, 1837–1840.
9. Amelard, R.; Glaister, J.; Wong, A.; Clausi, D.A. High-level intuitive features (HLIFs) for intuitive skin lesion description. *IEEE Trans. Biomed. Eng*. **2015**, *62*, 820–831.
10. Glaister, J.; Wong, A.; Clausi, D.A. Segmentation of skin lesions from digital images using joint statistical texture distinctiveness. *IEEE Trans. Biomed. Eng.* **2014**, *61*, 1220–1230.
11. Glaister, J.; Amelard, R.; Wong, A.; Clausi, D.A. MSIM: Multistage illumination modeling of dermatological photographs for illumination-corrected skin lesion analysis. *IEEE Trans. Biomed. Eng*. **2013**, *60*, 1873–1883.
12. Oliveira, R.B.; Filho, M.E.; Ma, Z.; Papa, J.P.; Pereira, A.S.; Tavares, J.M.R.S. Computational methods for the image segmentation of pigmented skin lesions: A review. *Comput. Method. Progr. Biomed.* **2016**, *131*, 127–141.
13. Mercedes Filho, M.; Ma, Z.; Tavares, J.M.R.S. A Review of the quantification and classification of pigmented skin lesions: From dedicated to hand-held devices. *J. Med. Syst.* **2015**, *39*, doi:10.1007/s10916-015-0354-8.
14. Ma, Z.; Tavares, J.M.R.S. Novel approach to segment skin lesions in dermoscopic images based on a deformable model. *IEEE J. Biomed. Health* **2016**, *20*, 615–623.
15. Oliveira, R.B.; Marranghello, N.; Pereira, A.S.; Tavares, J.M.R.S. A computational approach for detecting pigmented skin lesions in macroscopic images. *Expert. Syst. Appl.* **2016**, *61*, 53–63.
16. Pennisi, A.; Bloisi, D.D.; Nardi, D.; Giampetruzzi, A.R.; Mondino, C.; Facchianoc, A. Skin lesion computational diagnosis of dermoscopic images: Ensemble models based on input feature manipulation. *Comput. Meth. Prog. Bio.* **2017**, *149*, 43–53.
17. Rosado, L.; Vasconcelos, M.J.V.; Castro, R.; Tavares, J.M.R.S. *From Dermoscopy to Mobile Teledermatology. Dermoscopy Image Analysis*; CRC Press: Boca Raton, FL, USA, 2015.
18. Xu, L.; Jackowski, M.; Goshtasby, A.; Roseman, D.; Bines, S.; Yu, C.; Dhawan, A.; Huntley, A. Segmentation of skin cancer images. *Image Vis. Comput.* **1999**, *17*, 65–74.
19. Silveira, M.; Nascimento, J.C.; Marques, J.S.; Marcal, A.R.S.; Mendonca, T.; Yamauchi, S.; Maeda, J.; Rozeira, J. Comparison of segmentation methods for melanoma diagnosis in dermoscopy images. *IEEE J. Sel. Top. Signal Process* **2009**, *3*, 35–45.
20. Lee, T.; Ng, V.; Gallagher, R.; Coldman, A.; McLean, D. DullRazor: A software approach to hair removal from images. *Comput. Biol. Med*. **1997**, *27*, 533–543.
21. Available online: http://www.dermweb.com/dull_razor (accessed on 1 December 2017).
22. Wighton, P.; Lee, T.K.; Atkinsa, M.S. Dermoscopic hair disocclusion using inpainting. *Proc. SPIE Med. Imaging* **2008**, 1–8, doi:10.1117/12.770776.
23. Mirzaalian, H.; Lee, T.K.; Hamarneh, G. Hair enhancement in dermoscopic images using dual-channel quaternion tubularness filters and MRF-based multilabel optimization. *IEEE Trans. Image Process.* ***2014***, *23*, 5486–5496.
24. Satheesha, T.Y.; Satyanarayana, D.; Giriprasad, M.N. A pixel interpolation technique for curved hair removal in skin images to support melanoma detection. *J. Theor. App. Infor. Tech*. **2014**, *70*, 559565.
25. Abbas, Q.; Celebi, M.E.; Garcia, I.F. Hair removal methods: A comparative study for dermoscopy images. *Biomed. Signal Proces.* ***2011***, *6*, 395–404.
26. Available online: https://uwaterloo.ca/vision-image-processing-lab/research-demos/skin-cancer-detection (accessed on 1 December 2017).
27. Available online: https://challenge.kitware.com/#challenge/560d7856cad3a57cfde481ba (accessed on 1 December 2017).

28. Chang, W.-Y.; Huang, A.; Yang, C.-Y.; Lee, C.-H.; Chen, Y.-C.; Wu, T.-Y.; Chen, G.-S. Computer-aided diagnosis of skin lesions using conventional digital photography: A reliability and feasibility study. *PLoS ONE* **2013**, *8*, e76212, doi:10.1371/journal.pone.0076212.
29. Tuba, M. Multilevel image thresholding by nature-inspired algorithms: A short review. *Comput. Sci. J. Mold.* **2014**, *22*, 318–338.
30. Satapathy, S.C.; Raja, N.S.M.; Rajinikanth, V.; Ashour, A.S.; Dey, N. Multi-level image thresholding using Otsu and chaotic bat algorithm. *Neural Comput. Applic.* **2016**, doi:10.1007/s00521-016-2645-5.
31. Rajinikanth, V.; Couceiro, M.S. RGB histogram based color image segmentation using firefly algorithm. *Proced. Com. Sci.* **2015**, *46*, 1449–1457.
32. Samanta,S.; Acharjee, S.; Mukherjee, A.; Das, D.; Dey, N. In Ant Weight lifting algorithm for image segmentation, Proceedings of the IEEE International Conference on Computational Intelligence and Computing Research (ICCIC), Madurai, India, 26–28 December 2013; pp. 1–5, doi:10.1109/ICCIC.2013.6724160.
33. Rajinikanth, V.; Raja, N.S.M.; Satapathy, S.C. Robust color image multi-thresholding using between-class variance and cuckoo search algorithm. *Adv. Intell. Syst. Comput*. **2016**, *433*, 379–386.
34. Balan, N.S.; Kumar, A.S.; Raja, N.S.M.; Rajinikanth, V. Optimal multilevel image thresholding to improve the visibility of Plasmodium sp. in blood smear images. *Adv. Intell. Syst. Comput.* **2016**, *397*, 563–571.
35. Rajinikanth, V.; Raja, N.S.M.; Latha, K. Optimal multilevel image thresholding: An analysis with PSO and BFO algorithms. *Aust. J. Basic Appl. Sci.* **2014**, *8*, 443–454.
36. Raja, N.S.M.; Rajinikanth, V.; Latha, K. Otsu based optimal multilevel image thresholding using firefly algorithm. *Model. Sim. Engg.* **2014**, 794574, doi:10.1155/2014/794574.
37. Otsu, N. A threshold selection method from gray-level histograms. *IEEE Trans. Syst. Man Cybern.* **1979**, *9*, 62–66.
38. Satapathy, S.; Naik, A. Social group optimization (SGO): A new population evolutionary optimization technique. *Complex Intell. Sys.* **2016**, *2*, 173–203.
39. Naik, A.; Satapathy, S.C.; Ashour, A.S.; Dey, N. Social group optimization for global optimization of multimodal functions and data clustering problems. *Neural Comput. Applic.* **2016**, doi:10.1007/s00521-016-2686-9.
40. Dey, N.; Ashour, A.S.; Althoupety, A.S. Thermal Imaging in Medical Science. *Recent Advances in Applied Thermal Imaging for Industrial Applications*; IGI: New Delhi, India, 2017; pp. 87–117, doi:10.4018/978-1-5225-2423-6.ch004.
41. Moraru, L.; Moldovanu, S.; Culea-Florescu, A.-L.; Bibicu, D.; Ashour, A.S.; Dey, N. Texture analysis of parasitological liver fibrosis images. *Microsc. Res. Tech.* **2017**, doi:10.1002/jemt.22875.
42. Dey, N.; Ahmed, S.S.; Chakraborty, S.; Maji, P.; Das, A.; Chaudhuri, S.S. Effect of trigonometric functions-based watermarking on blood vessel extraction: An application in ophthalmology imaging. *Int. J. Embed. Sys*. **2017**, *9*, 90–100.
43. Ahmed, S.S.; Dey, N.; Ashour, A.S.; Sifaki-Pistolla, D.; Bălas-Timar, D.; Balas, V.E.; Tavares, J.M.R.S. Effect of fuzzy partitioning in Crohn's disease classification: A neuro-fuzzy-based approach. *Med. Biol. Eng. Comput.* **2017**, *55*, 101–115.
44. Ngan, T.T.; Tuan, T.M.; Minh, N.H.; Dey, N. Decision making based on fuzzy aggregation operators for medical diagnosis from dental x-ray images. *J. Med. Syst.* **2016**, *40*, 280, doi:10.1007/s10916-016-0634-y.
45. Dey, N.; Ashour, A.S.; Chakraborty, S.; Samanta, S.; Sifaki-Pistolla, D.; Ashour, A.S.; Le, D.-N.; Nguyen, G.N. Healthy and unhealthy rat hippocampus cells classification: A neural based automated system for alzheimer disease classification. *J. Adv. Microsc. Res.* **2016**, *11*, 1–10, doi:10.1166/jamr.2016.1282.
46. Kotyk, T.; Dey, N.; Ashour, A.S.; Balas-Timar, D.; Chakraborty, S.; Ashour, A.S.; Tavares, J.M.RS. Measurement of glomerulus diameter and Bowman's space width of renal albino rats. *Comput. Meth. Prog. Bio.* **2016**, *126*, 143–153.
47. Kausar, N.; Abdullah, A.; Samir, B.B.; Palaniappan, S.; Al Ghamdi, B.S.; Dey,N. Ensemble Clustering Algorithm with Supervised Classification of Clinical Data for Early Diagnosis of Coronary Artery Disease. *J. Med. Imaging Health Inf.* **2016**, *6*, 78–87.
48. Araki, T.; Ikeda, N.; Molinari, F.; Dey, N.; Acharjee, S.; Saba, L.; Nicolaides, A. Automated Identification of Calcium Coronary Lesion Frames From Intravascular Ultrasound Videos. *J. Ultrasound Med.* **2014**, *33*, S1–S124.

49. Kapur, J.N.; Sahoo, P.K.; Wong, A.K.C. A new method for gray-level picture thresholding using the entropy of the histogram. *Comput. Vis. Graph. Image Process.* **1985**, *29*, 273–285.
50. Lakshmi, V.S.; Tebby, S.G.; Shriranjani, D.; Rajinikanth, V. Chaotic cuckoo search and Kapur/Tsallis approach in segmentation of T. cruzi from blood smear images. *Int. J. Comp. Sci. Infor. Sec. (IJCSIS)* **2016**, *14*, 51–56.
51. Manic, K.S.; Priya, R.K.; Rajinikanth, V. Image multithresholding based on Kapur/Tsallis entropy and firefly algorithm. *Ind. J. Sci. Technol*. **2016**, *9*, doi:10.17485/ijst/2016/v9i12/89949.
52. Akay, B. A study on particle swarm optimization and artificial bee colony algorithms for multilevel thresholding. *Appl. Soft Comput*. **2013**, *13*, 3066–3091.
53. Bhandari, A.K.; Kumar, A.; Singh, G.K. Modified artificial bee colony based computationally efficient multilevel thresholding for satellite image segmentation using Kapur's, Otsu and Tsallis functions. *Expert Syst. Appl.* **2015**, *42*, 1573–1601.
54. Caselles, V.; Catte, F.; Coll, T.; Dibos, F. A geometric model for active contours in image processing. *Numer. Math*. **1993**, *66*, 1–31.
55. Malladi, R.; Sethian, J.A.; Vemuri, B.C. Shape modeling with front propagation: A level set approach. *IEEE Trans. Pattern Anal. Mac. Int.* **1995**, *17*, 158–175.
56. Li, C.; Xu, C.; Gui, C.; Fox, M.D. Distance regularized level set evolution and its application to image segmentation. *IEEE T. Image Process.* **2010**, *19*, 3243–3254.
57. Vaishnavi, G.K.; Jeevananthan, K.; Begum, S.R.; Kamalanand, K. Geometrical analysis of schistosome egg images using distance regularized level set method forautomated species identification. *J. Bioinform. Intell. Cont.* **2014**, *3*, 147–152.
58. Bresson, X.; Esedoglu, S.; Vandergheynst, P.; Thiran, J.-P.; Osher, S. Fast global minimization of the active contour/snake model. *J. Math. Imaging Vis.* **2007**, *28*, 151–167.
59. Chan, T.F.; Vese, L.A. Active contours without edges. *IEEE Trans. Image Process.* **2001**, *10*, 266–277.
60. Lankton, S.; Tannenbaum, A. Localizing region-based active contours. *IEEE Trans. Image Process.* **2008**, *17*, 2029–2039.
61. Chaddad, A.; Tanougast, C. Quantitative evaluation of robust skull stripping and tumor detection applied to axial MR images. *Brain Infor.* **2016**, *3*, 53–61.
62. Lu, H.; Kot, A.C.; Shi, Y.Q. Distance-reciprocal distortion measurefor binary document images. *IEEE Signal Process. Lett.* **2004**, *11*, 228–231.
63. Moghaddam, R.F.; Cheriet, M. A multi-scale framework for adaptive binarization of degraded document images. *Pat. Recognit*. **2010**, *43*, 2186–2198.
64. Mostafa, A.; Hassanien, A.E.; Houseni, M.; Hefny, H. Liver segmentation in MRI images based on whale optimization algorithm. *Multimed. Tools Appl.* **2017**, doi:10.1007/s11042-017-4638-5.
65. Sokolova, M.; Lapalme, G. A systematic analysis of performance measures for classification tasks. *Inf. Process. Manag*. **2009**, *45*, 427–437.
66. Demsar, J. Statistical comparisons of classifiers over multiple data sets. *J. Mach. Learn. Res*. **2006**, *7*, 1–30.